International Journal of Pharmaceutics 697 (2026) 126874

Contents lists available at ScienceDirect

International Journal of Pharmaceutics

journal homepage: www.elsevier.com/locate/ijpharm

Cholecalciferol-loaded electrospun coating on titanium-based implant for improved osseointegration

Francisca Acevedo [a,b,c,*], Jeyson Hermosilla [c], Alexis Vera [d], Felipe Galvez-Jirón [e], Vanessa Campos-Bijit [c,f], Rodrigo Navia [c,g,h], Nicolas Cohn [i], Pablo Navarro [j,k], Pablo Acuña-Mardones [l], Víctor Beltrán [m], Luis Diaz-Gomez [n], Maria Pita-Vilar [n], Iván Valdivia-Gandur [o], María Cristina Manzanares [p]

[a] Universidad de La Frontera, Faculty of Medicine, Department of Basic Sciences, Avenida Francisco Salazar 1145, 4780000 Temuco, Chile
[b] Universidad de La Frontera, Faculty of Medicine, Center of Excellence in Translational Medicine (CEMT), and Scientific and Technological Bioresource Nucleus (BIOREN), Avenida Francisco Salazar 1145, 4780000 Temuco, Chile
[c] Millennium Nucleus Bioproducts, Genomics and Environmental Microbiology (BioGEM), Avenida España 1680, 2390123 Valparaíso, Chile
[d] Universidad de La Frontera, Faculty of Dentistry, Master in Dentistry, Avenida Francisco Salazar 1145, 4780000 Temuco, Chile
[e] Universidad de La Frontera, Faculty of Medicine, Programa de Doctorado en Ciencias, mención Biología Celular y Molecular aplicada, Avenida Francisco Salazar 1145, 4780000 Temuco, Chile
[f] Universidad de Chile, Faculty of Dentistry, Research Institute of Dental Science, Laboratory of Nanobiomaterials, 8380544 Santiago, Chile
[g] Universidad San Sebastián, Faculty of Engineering, Bellavista 7, Santiago, Chile
[h] Center for Advancing Agri-Food System Transformation, Santiago, Chile
[i] Instituto Universitario de Investigación y Desarrollo Tecnológico (IDT), Ignacio Valdivieso 2409, 8940000 Santiago, Chile
[j] Universidad de La Frontera, Faculty of Dentistry, Dental Science Research Center (CICO), Avenida Francisco Salazar 1145, 4780000 Temuco, Chile
[k] Universidad Autónoma de Chile, Faculty of Health Sciences, 4810101 Temuco, Chile
[l] Universidad de La Frontera, Faculty of Medicine, Programa de Doctorado en Ciencias Morfológicas, Avenida Francisco Salazar 1145, 4780000 Temuco, Chile
[m] Universidad de La Frontera, Faculty of Dentistry, Clinical Investigation and Dental Innovation Center (CIDIC), Avenida Francisco Salazar 1145, 4780000 Temuco, Chile
[n] Departamento de Farmacología, Farmacia y Tecnología Farmacéutica, I+D Farma (GI-1645), Facultad de Farmacia, Instituto de Materiales (iMATUS) and Health Research Institute of Santiago de Compostela (IDIS), Universidade de Santiago de Compostela 15782 Santiago de Compostela, Spain
[o] Universidad de Antofagasta, Biomedical Department, Avenida Angamos 601, Antofagasta, Chile
[p] University of Barcelona, Faculty of Medicine and Health Sciences, Experimental Pathology and Therapeutics Department, Human Anatomy and Embryology Unit, Barcelona, Spain

ARTICLE INFO

Keywords:
Cholecalciferol
Drug delivery coating
Electrospun nanofibers
Osseointegration
Poly(ε-caprolactone) (PCL)
Titanium implants

ABSTRACT

As the global population ages, the need for biomaterials capable of supporting bone repair and regeneration is steadily increasing. Particularly, enhancing early peri-implant bone regeneration remains a key challenge in implant therapy, particularly in situations requiring improved biological responsiveness at the implant surface. In this study, cholecalciferol-loaded poly(ε-caprolactone) (PCL) nanofiber meshes were fabricated by electrospinning to create conformal, homogeneous drug delivery coatings on titanium mini-implants. The electrospun meshes exhibited uniform fiber morphology, consistent thickness control, and mechanical properties required for handling and implantation. Cholecalciferol was successfully incorporated into the PCL matrix and released in a sustained manner. *In vitro* studies using MSCs and MG-63 cells showed that the coatings were cytocompatible and supported osteogenic activity, including increased ALP activity, collagen, and mineralized extracellular matrix deposition. In a rat tibia model, Ti mini-implants coated with the cholecalciferol-loaded PCL meshes exhibited improved early peri-implant bone formation, exhibiting higher bone volume and a denser trabecular microarchitecture compared with uncoated implants, without eliciting systemic or local toxicity. In conclusion, localized cholecalciferol release from nanofibrous PCL coatings can be used as an effective strategy to modulate early peri-implant biology and accelerate implant osseointegration.

* Corresponding author.
E-mail address: francisca.acevedo@ufrontera.cl (F. Acevedo).

https://doi.org/10.1016/j.ijpharm.2026.126874
Received 3 March 2026; Received in revised form 10 April 2026; Accepted 12 April 2026
Available online 14 April 2026

1. Introduction

The long-term success of dental implants depends on achieving rapid and stable osseointegration between the implant surface and the surrounding bone (Geetha et al., 2009). Despite improvements in implant design and surface topography, insufficient peri-implant bone formation and early bone resorption are still common causes of implant failure, especially in challenging healing situations (Abd-Elaziem et al., 2024). This has led to increasing interest in surface modifications that do more than provide mechanical stability and instead actively support bone regeneration at the implant-bone interface (Wang et al., 2016).

Successful osseointegration depends on the coordinated recruitment of osteoblasts, extracellular matrix (ECM) deposition, and balanced bone remodeling during the early healing phase (Agarwal & García, 2015). These processes are strongly influenced by implant surface properties through their effects on protein adsorption, cell adhesion, and osteogenic differentiation (Chen et al., 2025; Dohan Ehrenfest et al., 2010). Although micro- and nanoscale surface topographical modifications, including etching, anodization, laser texturing, and calcium phosphate-based coatings, have shown to enhance bone-implant contact and support early osteogenic cell attachment, their biological impact remains strongly influenced by host bone quality and healing conditions (Coelho et al., 2015; Palmquist et al., 2010). Increasing evidence indicates that surface topography alone may be insufficient to ensure predictable osseointegration in compromised environments, including osteoporotic bone, irradiated tissue, or conditions associated with impaired angiogenesis and dysregulated bone remodeling (Colnot et al., 2007; García-de-Albeniz et al., 2023; Smeets et al., 2016). Here, topographical cues primarily provide passive osteoconductive support and do not adequately modulate the complex biological events governing early peri-implant healing, such as inflammatory signaling and the balance between osteogenesis and bone resorption (Hussain et al., 2024; Pandey et al., 2022). As a result, biomaterial-based implant coatings capable of locally delivering osteoactive signals have gained growing attention as a strategy to enhance peri-implant bone regeneration and improve implant integration under clinically challenging conditions (Bohara & Suthakorn, 2022; Talebian et al., 2023).

In this context, electrospinning has emerged not only as a surface modification technique, but also as a versatile platform for local drug delivery. Electrospun nanofibrous meshes replicate key structural features of the bone extracellular matrix while providing high surface area and interconnected porosity, enabling both intimate interaction with bone tissue and controlled release of incorporated bioactive molecules (Ding et al., 2019). Moreover, electrospun fibrous meshes offer a suitable carrier system for localized delivery of therapeutic agents at the bone-implant interface, as bioactive molecules can be physically entrapped within the polymer matrix and released in a sustained, diffusion-controlled manner (Gedik & Erdem, 2025). Multiple studies have demonstrated that drug-loaded electrospun nanofibrous coatings actively enhance osseointegration when applied to metallic implant surfaces (Das et al., 2019). Osteogenic electrospun nanofibrous coatings on titanium implants have been shown to significantly improve bone–implant integration *in vivo*, with increased peri-implant bone formation and stronger interfacial bonding compared with uncoated implants (Das et al., 2018). Similarly, coaxial electrospun nanofiber coatings incorporating doxycycline enabled sustained local drug release, reduced bacterial colonization, and resulted in significantly improved osseointegration in a rat implant model (Song et al., 2017). More broadly, electrospun fibrous layers incorporating collagen, hydroxyapatite, and antimicrobial agents have been reported to preserve peri-implant bone structure and promote osseointegration by synergistically combining an ECM-mimetic architecture with localized therapeutic delivery (Dieterle et al., 2022; Nhlapo et al., 2022).

Cholecalciferol, or vitamin D_3 (Chol), is a particularly attractive osteoactive molecule for localized delivery. Chol plays a central role in skeletal homeostasis by regulating calcium and phosphate metabolism, promoting osteoblast differentiation, and modulating bone remodeling through effects on osteoblast–osteoclast signaling, including RANKL-mediated pathways (Belgheisi et al., 2020; Christakos et al., 2016). Clinical and preclinical studies have consistently associated Chol deficiency with impaired peri-implant bone healing and increased implant failure risk, particularly during the early stages of osseointegration (Miron et al., 2025). However, several studies have reported that systemic vitamin D supplementation produces inconsistent effects on early osseointegration, likely due to limited control over local vitamin D availability at the bone-implant interface during the critical early healing phase (Jo et al., 2024; Miron et al., 2025). Therefore, incorporating Chol into electrospun nanofibrous implant coatings, where sustained local release from an ECM-mimetic architecture, may amplify osteogenic signaling at the implant surface while minimizing systemic exposure. In addition, Chol has been reported to exert antimicrobial and immune-modulatory effects through both direct actions on bacterial membranes and indirect stimulation of host defense peptides (Golpour et al., 2019).

This study aims to investigate the effectiveness of Chol-loaded electrospun PCL meshes applied as surface coatings on Ti screw-type implants to promote sustained local Chol delivery at the bone-implant interface. The central hypothesis is that covering Ti screws with a fibrous electrospun PCL coating capable of controlled Chol release would enhance osteogenic differentiation, mitigate adverse bone remodeling, and ultimately improve *peri*-implant bone formation and osseointegration. The coating was engineered to provide a nanoscale fibrous architecture while enabling sustained, localized Chol release directly from the implant surface. Osteogenic responses were evaluated *in vitro* using mesenchymal stem cells and MG-63 osteoblast-like cells, while *in vivo* osseointegration was assessed using Chol-loaded PCL-coated screw implants placed in the proximal tibial metaphysis of Sprague-Dawley rats.

2. Material and methods

2.1. Materials

PCL (80 kDa), alizarin red staining, and MTT reagent were from Sigma Aldrich Co. (St Louis, MO, USA). The alkaline phosphatase assay kit (BCIP-NBT), Chol, dexamethasone, potassium phosphate monobasic, ascorbic acid, chloroform, and formaldehyde were from Merck (Darmstadt, Germany). Dulbecco's phosphate saline buffer (DPBS), α-MEM medium, fetal bovine serum (FBS), penicillin and streptomycin, and Trypsin-EDTA were from HyClone (USA). Bone screws (Ti mini-implant) were from BIO Materials Korea (Seoul, Korea), and distributed in Chile by Biomateriales Chile (Providencia, Chile).

2.2. Preparation of polymeric solutions and electrospinning

Polymeric solutions were prepared by dissolving poly (ε-caprolactone) (PCL) in chloroform to obtain a final concentration of 14% (w/v). Cholecalciferol-loaded formulations (Chol-PCL) were prepared by incorporating cholecalciferol (Chol) into the PCL solution at concentrations of 0.1% and 0.5% (w/v), respectively. All solutions were magnetically stirred until complete dissolution and homogeneous dispersions were obtained. The viscosity and torque of the polymeric solutions were measured using a DVNext Brookfield rheometer (AMETEK, Middleboro, MA, USA). For each formulation, 100 mL of solution was transferred into a beaker and analyzed using spindle No. 03 (3.5 cm diameter) at room temperature. Measurements were conducted at a constant rotational speed of 200 rpm for 2 min.

Electrospun meshes were fabricated using a NEU-BM electrospinning system (Tong Li Tech, Shenzhen, China) under ambient conditions (20 °C, 50% relative humidity). Electrospinning was carried out at an applied voltage of 25 kV, solution flow rate of 2 mL/h, tip-to-collector distance of 20 cm, and collector rotation speed of 50 rpm, following a previously described protocol (Sanhueza et al., 2023). Based on our

previous findings (Beltrán et al., 2023 PCT/CL2023/050141; Sanhueza et al., 2023), we selected cholecalciferol concentrations of 0.1% and 0.5% (w/v) for the fabrication of electrospun PCL and Chol-PCL meshes. Additionally, based on preliminary laboratory data, we defined two target thicknesses—25 and 50 μm—to systematically evaluate the influence of coating thickness on the resulting material properties and biological performance. Thickness was controlled by adjusting the electrospinning time to 15 and 30 min, respectively. The electrospinning times (15 and 30 min) were empirically determined from previous experiments in our laboratory, which demonstrated a consistent correlation between spinning duration and the resulting coating thickness under the selected processing conditions. These thicknesses were established according to multiple practical and experimental criteria derived from prior laboratory optimization studies, including achieving a coating that did not significantly interfere with the surgical handling and implantation procedure, ensuring sufficient mechanical integrity to prevent damage during surgical manipulation, and obtaining the desired thickness within a reasonably short and operationally efficient electrospinning time.

2.3. Coating of titanium mini-implants

Commercially available medical-grade titanium (Ti) bone screws were used as implant substrates. The screws had a total length of 7 mm, a core diameter of 1.50 mm, and a head diameter of 2.5 mm. The implant geometry was selected based on preliminary optimization studies (**Table S1 and Figure S1, Supplementary Material**).

Ti mini-implants were coated with electrospun PCL fibers, either non-loaded or loaded with cholecalciferol (0.5% w/v). Coatings were applied at two nominal thicknesses (25 and 50 μm), corresponding to electrospinning times of 15 and 30 min, respectively, using the same electrospinning parameters described in Section 2.2. During coating, Ti screws were mounted on the rotating collector to ensure uniform and conformal deposition of fibers over the threaded geometry. After electrospinning, coated implants were allowed to dry under ambient conditions (~ 20 °C) to ensure complete solvent evaporation prior to subsequent characterization and biological evaluation.

2.4. Physicochemical characterization of electrospun meshes and coatings

2.4.1. Morphology and fiber diameter analysis

Fiber morphology and diameter were assessed using scanning electron microscopy (SEM; Hitachi SU2500, Hitachi High-Tech, Japan). Prior to imaging, samples ($n = 3$) were sputter-coated with an 8 nm layer of gold using an AUTO 108 argon sputter coater (Cressington Scientific Instruments Ltd., Watford, UK).

SEM images were analyzed using ImageJ software (National Institutes of Health, USA) to determine fiber diameter and morphology. A minimum of 20 segments per sample were measured from randomly selected regions. High-resolution imaging was further performed using field-emission SEM (FE-SEM; GeminiSEM 360, Carl Zeiss AG, Oberkochen, Germany).

2.4.2. Surface topography and roughness

Surface topography of different electrospun meshes was characterized using atomic force microscopy (AFM; CoreAFM, NanoSurf, Switzerland). Measurements were performed in contact and dynamic force modes using scan areas of 19 × 19 μm^2 and 20 × 20 μm^2. For each sample, three independent regions ($n = 3$) were analyzed. Surface roughness was quantified as arithmetic mean roughness (Sa). Data processing was carried out using Gwyddion software (v2.95).

2.4.3. Thermal properties

Thermal analyses were performed using thermogravimetric analysis (TGA) and differential scanning calorimetry (DSC) with a STA 6000 system (PerkinElmer Inc., Waltham, MA, USA). Samples (~20 mg) were analyzed under nitrogen at a flow rate of 40 mL/min and heated from 25 °C to 600 °C at 15 °C/min. Glass transition temperature (Tg), melting temperature (Tm), and enthalpy of fusion (ΔH) were determined.

2.4.4. FTIR-ATR

FTIR-ATR spectra were recorded using a Cary 630 FTIR spectrometer (Agilent Technologies Inc., Danbury, CT, USA) over the range of 600–4000 cm^{-1} at a resolution of 0.96 cm^{-1}.

2.5. Mechanical characterization

Electrospun meshes ($n = 3$) were cut into rectangular specimens (40 × 10 mm) and tested in tension using a CT3 digital texture analyzer (Brookfield AMETEK, Middleboro, MA, USA). Tests were performed at 20 °C using a gauge length of 8.0 mm and a crosshead speed of 0.1 mm/s. Tensile modulus, ultimate tensile strength, and elongation at break were calculated from stress-strain curves.

2.6. Chol release

The release of Chol from electrospun meshes was evaluated following the protocol described by (da Silva et al., 2021). Briefly, 100 mg of Chol-loaded PCL meshes (25 μm thickness, 0.5% w/v Chol) were immersed in 20 mL of PBS (pH = 7.4, supplemented with 0.5 v/v% Tween 80) and incubated at (37 °C, static conditions). At predetermined time points, 1 mL aliquots of the release medium were withdrawn and replaced with an equal volume of fresh PBS. The amount of Chol released was quantified by measuring the absorbance of the collected aliquots using a UV–Vis spectrophotometer at a wavelength of 266 nm. PCL meshes without Chol were used as negative controls to account for background absorbance, while free Chol in PBS at different concentrations served as a calibration curve (3.9, 7.8, 15.6, 33, 35 and 37 mg/L). All experiments were performed in triplicate ($n = 3$).

Release profiles were expressed as cumulative released mass (mg) and as percentage of the total cholecalciferol content incorporated into the membranes. To elucidate the release mechanism, the experimental data were fitted to different kinetic models, namely zero-order, first-order, Higuchi, and Korsmeyer-Peppas.

2.7. In vitro biocompatibility assays

MG-63 osteoblast-like cells and bone marrow-derived mesenchymal stem cells (MSCs) were used to evaluate biocompatibility. MG-63 cells and MSCs were cultured in α-minimum essential medium (α-MEM) supplemented with 10% (v/v) fetal bovine serum (FBS) and 1% (v/v) penicillin–streptomycin (HyClone, Danaher Corporation, Washington D. C., USA). Cells were incubated at 37 °C in a humidified atmosphere containing 5% CO_2. Upon reaching approximately 90% confluency, cells were detached using 0.25% (w/v) trypsin-EDTA (Corning, Promenade, Singapore) for 3 min, neutralized with complete medium, and collected by centrifugation. Cells were then seeded into 24-well tissue culture plates at a density of 1 × 10^4 cells per well in 500 μL of complete medium.

For cell viability and proliferation studies, electrospun fiber discs (6 mm diameter; $n = 5$) with thicknesses of 25 or 50 μm, either unloaded or loaded with cholecalciferol (0.1% or 0.5% w/v), were sterilized by ozone treatment for 30 min. After cell seeding, the sterilized fiber discs were placed into the wells in direct contact with the culture medium. Seeded wells containing complete medium without discs served as controls. Cell viability and proliferation were assessed after 1, 3, and 7 days of incubation using an MTT assay, following the manufacturer's protocol, as was reported by Jeon et al. (2014), with some modifications.

2.8. Evaluation of osteogenic activity in vitro

To evaluate the osteogenic potential of the electrospun scaffolds,

MSCs and MG-63 cells were cultured as described in Section 2.6. Cells were seeded onto PCL meshes (6 mm diameter; $n = 5$ per condition) with thicknesses of 25 or 50 μm, either unloaded or loaded with cholecalciferol (0.1% or 0.5% w/v). Seeding was performed in 24-well plates at a density of 1×10^4 cells per mesh in 500 μL of complete MEM-α, followed by a 24 h incubation period to allow cell attachment. After this initial attachment phase, the culture medium was replaced according to the experimental condition. For the osteogenic condition, cells were maintained in complete MEM-α supplemented with 50 μg/mL ascorbic acid and 10 mM β-glycerophosphate (adapted from Langenbach & Handschel, 2013). In parallel, cells were cultured under non-osteogenic conditions in MEM-α supplemented only with FBS and penicillin/streptomycin, as described in Section 2.6. Extracellular matrix production and mineralization were evaluated as indicators of osteogenic activity under both culture conditions.

2.8.1. Calcium deposition

Calcium deposition was quantified on day 21 by Alizarin Red S staining following a modified protocol based on Gregory et al. (2004). Samples were fixed with 4% paraformaldehyde, stained with 40 mM Alizarin Red S for 30 min, and washed with PBS. The bound dye was extracted with 10% (v/v) acetic acid at 80 °C for 15 min, neutralized with 10% (v/v) ammonium hydroxide, and centrifuged at 20,000 g for 15 min. Absorbance of the supernatant was measured at 405 nm in triplicate.

To assess relative osteogenic induction, absorbance values were normalized to untreated cells cultured in basal medium (without scaffold) and expressed as fold change relative to control.

2.8.2. Collagen deposition

Collagen deposition was assessed on days 7, 14, and 21 using Sirius Red staining following a modified protocol based on Walsh et al. (1992). Fixed samples were incubated in 1 mL of Sirius Red solution for 1 h, rinsed with deionized water, and imaged under bright-field microscopy. Bound dye was eluted using a 0.2M NaOH:methanol solution (1:1) under gentle agitation for 30 min, transferred to 96-well plates, and quantified by measuring absorbance at 405 nm.

2.8.3. Alkaline phosphatase activity

The alkaline phosphatase activity was measured using an alkaline phosphatase assay kit (BCIP-NBT; Sigma-Aldrich, St. Louis, MO, USA) following an adapted protocol as reported by Pereira et al. (2014), with some modifications. ALP activity, an early marker of osteogenic differentiation, was quantified on days 7, 14, and 21 under both osteogenic and non-osteogenic conditions. After 7, 14 and 21 days of incubation, wells were carefully washed twice with PBS. Then, 500 μL of the working solution was added to each well, and the plate was incubated for 2 h at 37 °C. The black-purple precipitate was then solubilized in 500 μL of isopropanol per well. Subsequently, 100 μL of the solution from each well was transferred in duplicate to a flat-bottomed 96-well plate. The optical density of the solution was measured at 595 nm using a plate microreader.

2.9. Animal studies

2.9.1. Experimental animal surgery

All animal procedures were approved by the Scientific Ethics Committee of the Universidad de La Frontera (CEC_UFRO Folio N°059/23) and conducted in accordance with Chilean regulation for care and use of animals in experimental procedures and ARRIVE guidelines.

Twenty-one adult male Sprague–Dawley rats (16–18 weeks old; 300–350 g) were randomly assigned to three experimental groups ($n = 7$ per group): (i) uncoated Ti mini-implants with a machined surface (control), (ii) Ti mini-implants coated with 0.5% w/v Chol-PCL meshes with a thickness of 25 μm, and (iii) Ti mini-implants coated with 0.5% w/v Chol-PCL meshes with a thickness of 50 μm. Animals were anesthetized by intraperitoneal injection of ketamine (100 mg/kg) and xylazine (13 mg/kg), followed by sevoflurane inhalation (250 mg) to maintain deep anesthesia. Prophylactic antibiotic treatment was administered subcutaneously using enrofloxacin (5 mg/kg) one hour prior to surgery. After shaving and disinfection, a 15 mm longitudinal incision was made over the proximal tibia, and soft tissues were bluntly dissected to expose the cortical bone. A pilot hole was drilled using a 1.5 mm drill bit, followed by a 1.8 mm drill to accommodate the 1.5 × 7 mm Ti mini-implant, which was inserted unilaterally into the proximal metaphysis (Vera-Becerra et al., 2026). Primary implant stability was confirmed manually using the BMK® Microscrew Kit grasper.

Soft tissues were closed using 5-0 absorbable sutures, and a 2% chlortetracycline topical spray was applied to prevent infection and self-trauma. Postoperative analgesia was provided by subcutaneous administration of ketoprofen (5 mg/kg) every 24 h for 72 h (Vera-Becerra et al., 2026). Animals were housed individually and monitored daily for the first two weeks, then every three days until study completion. No mortality was observed throughout the entire experimental period.

After 31 days, animals were euthanized by overdose of ketamine–xylazine anesthesia followed by bilateral pneumothorax (Vera-Becerra et al., 2026). Tibiae containing the implants were harvested and fixed in 10% neutral buffered formaldehyde for 48 h prior to histological and histomorphometric analyses.

2.9.2. Toxicological evaluation

To assess potential systemic toxicity associated with the implanted devices, serum biochemical parameters related to renal and hepatic function and bone mineral metabolism were evaluated. Blood samples were collected at the time of euthanasia by cardiac puncture under aseptic conditions using 1 mL syringes equipped with 25G needles. Samples were allowed to clot for 15 min at room temperature, transferred on dry ice to the laboratory, and stored at −20 °C until analysis.

Standard clinical biochemistry methods were used to quantify calcium, phosphorus, creatinine, blood urea nitrogen, albumin, alanine aminotransferase, aspartate aminotransferase, alkaline phosphatase, and uric acid levels (Sharp & Villano, 2012).

2.9.3. MicroCT analysis

Micro-computed tomography (microCT) analysis was performed using a SkyScan 1273 system (Bruker, Kontich, Belgium). Scanning was conducted using a voltage of 125 kV, current of 64 μA, exposure time of 3500 ms, and a 1 mm Cu filter (Vera-Becerra et al., 2026). The resulting isotropic voxel size was 9 μm. Reconstruction was performed using NRecon software (v2.2.0.6, Bruker), applying ring artifact correction (5), beam hardening correction (59%) and smoothing (5). Reconstructed datasets were aligned in coronal, sagittal, and transaxial planes using DataViewer software (v1.5.6.2, Bruker). Segmentation and quantitative analyses were conducted using CTAn software (Bruker). For each sample, a concentric cylindrical volume of interest (VOI) was defined immediately below the Ti mini-implant head. The VOI measured 2 mm in height and 1.2 mm in radius and was positioned tangential to the implant crests while excluding the implant volume, thereby encompassing the peri-implant bone region.

Segmentation threshold for Ti mini-implant used a grayscale intensity range of 70–235, while mineralized bone tissue was 37–63. Bone mineral density (BMD) calibration was performed using hydroxyapatite phantoms (Bruker) with densities of 0.30 and 1.25 g/cm^3. Quantitative structural parameters included bone volume, bone volume fraction (BV/TV, %), trabecular thickness, trabecular separation, and porosity. All measurements were performed by a trained examiner blinded to the experimental groups to minimize bias.

2.9.4. Histomorphometric analysis by BS-SEM

Following micro-CT, samples were embedded in Technovit® resin and sectioned longitudinally along the implant axis using an Exact®

diamond saw to obtain ~ 0.2 mm slices. BS-SEM preparation followed established protocols (Valdivia-Gandur et al., 2016). Quantitative analysis was performed within a rectangular ROI centered on the implant, defined by the implant length-to-diameter ratio (7:2.5 = 2.8) with a 5% width increase to ensure peri-implant tissue inclusion. Cortical bone was excluded; trabecular bone from cortical margins and newly formed bone in inter-thread regions were included. The relative amounts of lamellar, fibroreticular, and chondroid bone were quantified to assess tissue maturation and peri-implant bone quality (Beltrán et al., 2020; Valdivia-Gandur et al., 2016). Image analysis was performed using ImageJ software (National Institutes of Health, USA).

2.10. Statistical analysis

All quantitative data are presented as mean ± standard deviation. Statistical analyses were performed using GraphPad Prism 9 (GraphPad Software, San Diego, CA, USA) and IBM SPSS Statistics (v29.0, IBM Corp., Armonk, NY, USA), depending on the analysis type. Normality of data distribution was assessed using the Shapiro-Wilk test, and homogeneity of variances was evaluated using Levene's test. One-way analysis of variance (ANOVA) was applied to assess differences among experimental groups, followed by Tukey's post-hoc test for pairwise comparisons where appropriate. Independent-samples t-tests were additionally used for specific pairwise comparisons when applicable. A value of $p < 0.05$ was considered statistically significant ($p < 0.05$; $p < 0.01$; $p < 0.001$; $p < 0.0001$).

3. Results and discussion

3.1. Effect of cholecalciferol on rheological properties of PCL solutions

The rheological behavior of polymeric solutions plays a critical role in electrospinning stability and fiber formation. The viscosity and torque of 14% (w/v) PCL solutions, either unloaded or containing cholecalciferol at 0.1% and 0.5% (w/v), are summarized in Table 1. The unloaded PCL solution exhibited the highest viscosity (873.7 ± 1.2 cP). Incorporation of cholecalciferol resulted in a concentration-dependent reduction in viscosity, decreasing to 842.7 ± 1.5 cP and 836.3 ± 0.6 cP at 0.1% and 0.5% (w/v), respectively. A similar trend was observed for torque values, which decreased from 87.3% for the unloaded PCL solution to 84.4% and 83.7% with increasing cholecalciferol content. All measurements were conducted at comparable temperatures (22–23 °C), indicating that the observed changes were primarily attributable to formulation composition rather than thermal effects.

The reduction in viscosity and torque suggests that cholecalciferol interferes with intermolecular interactions within the PCL solution, leading to reduced flow resistance. Similar effects have been reported when low-molecular-weight hydrophobic additives are incorporated into polymer solutions, where plasticization or disruption of chain entanglements facilitates easier jet elongation during electrospinning. From a processing standpoint, these rheological changes are advantageous, as they promote stable jet formation and reduce the likelihood of defects, thereby supporting the production of uniform fibrous meshes. The maintained viscosity range further indicates that cholecalciferol incorporation did not compromise solution spinnability, consistent with earlier reports on electrospun composite systems (Douglas et al., 2016; Dumitriu et al., 2021; Paxton et al., 2019).

Table 1
Viscosity and torque results of PCL solutions, and PCL solution mixed with 0.1 or 0.5 w/v% Chol.

Polymeric solutions	Viscosity (cP)	Torque (%)	Temperature (°C)
14% (w/v) PCL	873.7 ± 1.2	87.3	23.1
14% (w/v) PCL with 0.1% (w/v) Chol	842.7 ± 1.5	84.4	22.0
14% (w/v) PCL with 0.5% (w/v) Chol	836.3 ± 0.6	83.7	22.5

3.2. Morphology and surface properties of electrospun PCL and Chol-PCL meshes

Electrospinning of unloaded PCL and cholecalciferol-loaded PCL formulations at 25 μm and 50 μm thickness resulted in continuous, randomly oriented fibrous meshes without the presence of beads or significant structural defects (Fig. 1). These observations indicate stable electrospinning conditions across all formulations and confirm that Chol incorporation did not adversely affect fiber formation.

3.2.1. Fiber morphology

Quantitative SEM analysis revealed fiber diameters ranging from 1.448 ± 0.293 μm to 1.766 ± 0.421 μm across all experimental groups (Table 2). Cholecalciferol-loaded meshes exhibited a slight tendency toward reduced fiber diameters compared to unloaded PCL controls; however, these differences were not statistically significant ($p > 0.05$).

The modest reduction in fiber diameter observed in cholecalciferol-loaded meshes can be correlated with the lower solution viscosity measured prior to electrospinning. Reduced viscosity facilitates greater jet stretching under the applied electric field, which can result in finer fibers, as previously described for electrospun polymer systems containing low-molecular-weight additives. Notably, the fiber diameters obtained in this study were smaller than those reported by Sanhueza et al. (2023) for analogous PCL systems, suggesting that the combined optimization of solution properties and electrospinning parameters favored enhanced fiber refinement.

The morphology index (MI), employed as an indicator of fiber uniformity and structural integrity, ranged from 0.55 to 0.95 across all conditions (Table 2). Meshes fabricated with a nominal thickness of 25 μm consistently showed high MI values (≥ 0.80), independent of cholecalciferol loading, indicating uniform, well-defined fibrous architectures.

In contrast, meshes collected at a thickness of 50 μm exhibited greater variability in MI values, particularly in cholecalciferol-loaded groups. This trend likely reflects subtle fluctuations in jet stability during prolonged electrospinning times required to achieve thicker mats. Nevertheless, all meshes maintained acceptable morphological quality, and no statistically significant differences were detected among groups. While extended electrospinning duration may introduce slight heterogeneity, fiber integrity remains preserved even in thicker coatings.

3.2.2. Surface topography and roughness

Surface topography analysis by AFM revealed that all electrospun meshes exhibited moderately rough surfaces (Fig. 1), with no statistically significant differences among unloaded and cholecalciferol-loaded formulations or between thicknesses (**Figure S2, Supplementary Material**). Although a higher variability was observed for PCL-0.5 Chol-25 μm, no statistically significant differences were detected between unloaded and cholecalciferol-loaded formulations or among the different coating thicknesses. Three-dimensional AFM reconstructions showed a micrometer-scale landscape characterized by peaks and valleys with height variations below approximately 1.5 μm. The presence of this microrough topography is inherent to electrospun fibrous architectures and is considered beneficial for bone-related applications, as surface roughness in the micro- and submicrometer range has been associated with enhanced osteogenic cell adhesion and differentiation. The slightly higher local variability observed in the PCL-0.5 Chol mesh at 25 μm thickness likely reflects localized fiber overlap rather than systematic differences in surface structure (Anjum et al., 2022; Cheng et al., 2017).

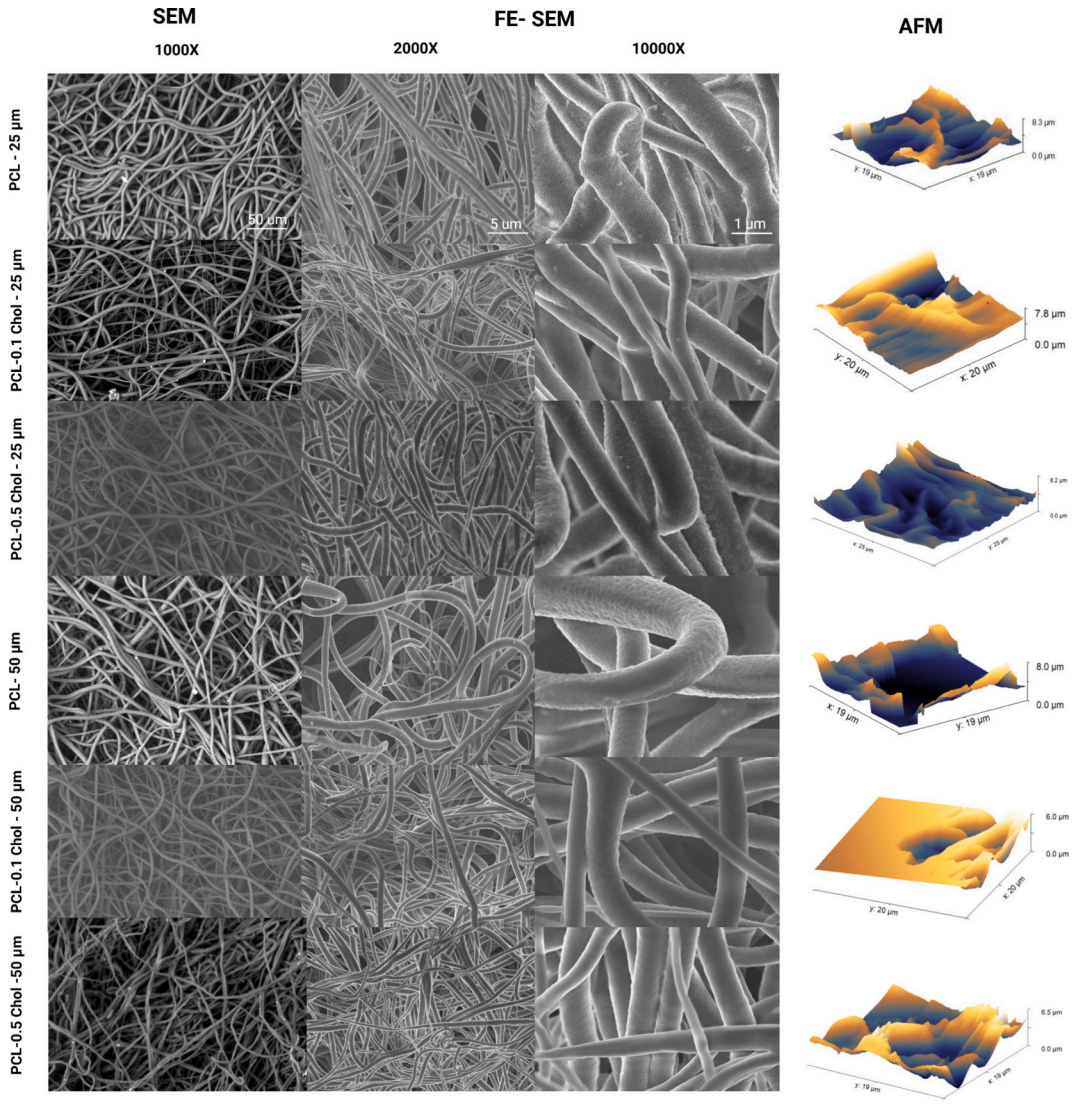

Fig. 1. SEM, FE-SEM and AFM images of nanofibers: Micrographs of the nanofibers are observed at different magnifications using SEM and FE-SEM. In addition, the three-dimensional (3D) roughness profiles of the samples are shown.

Table 2
Mean diameter and morphology index of the obtained electrospun fibers.

Fibers	**Fiber diameter** (µm)	**Morphology Index** (MI)
PCL- 25 µm	1.766 ± 0.421	0.95
PCL-0.1 Chol – 25 µm	1.563 ± 0.374	0.80
PCL-0.5 Chol – 25 µm	1.611 ± 0.290	0.95
PCL- 50 µm	1.645 ± 0.261	0.90
PCL-0.1 Chol – 50 µm	1.597 ± 0.324	0.75
PCL-0.5 Chol –50 µm	1.448 ± 0.293	0.55

3.3. Physicochemical characterization of electrospun PCL and Chol-PCL meshes

3.3.1. Thermal properties

Thermal analysis was conducted to evaluate the stability and phase behavior of the electrospun PCL and Chol-PCL meshes. The TGA profiles (Fig. 2A, Table 3) showed a single, well-defined weight-loss event between 350 and 450 °C for all formulations, corresponding to degradation of the PCL matrix, in agreement with previous reports on electrospun PCL systems (Schulze et al., 2012). The temperature at which this main degradation occurred was similar across most samples (approximately 419–421 °C). The only exception was the PCL-0.5 Chol mesh at 50 µm, which showed a lower degradation temperature (397.57 °C). Because this deviation does not correlate with cholecalciferol content or coating thickness, it is most likely due to normal experimental variability rather than a formulation-driven effect. Overall, the incorporation of cholecalciferol did not reduce the thermal stability of the coatings.

DSC (Fig. 2B) revealed melting transitions between 55 and 60 °C in all groups, characteristic of semicrystalline PCL. A slight increase in melting temperature was observed in cholecalciferol-loaded meshes, most notably in the PCL-0.5 Chol mesh at 25 µm (59.73 °C compared with 55.09 °C in unloaded PCL), suggesting modest alterations in crystalline packing.

The most notable changes appeared in the degree of crystallinity (Table 3). The addition of cholecalciferol substantially reduced crystallinity in both thickness groups: from 21.86% to 11.50% in the 25 µm meshes, and from 17.16% to 12.16% in the 50 µm meshes. These reductions indicate that cholecalciferol interferes with PCL chain packing and limits lamellar organization during solidification, a trend previously described in electrospun systems containing low-molecular-weight hydrophobic additives (Cai et al., 2014; Sanhueza et al., 2023). This decrease in crystallinity may influence how the coating behaves in biological environments. Lower crystallinity typically promotes faster

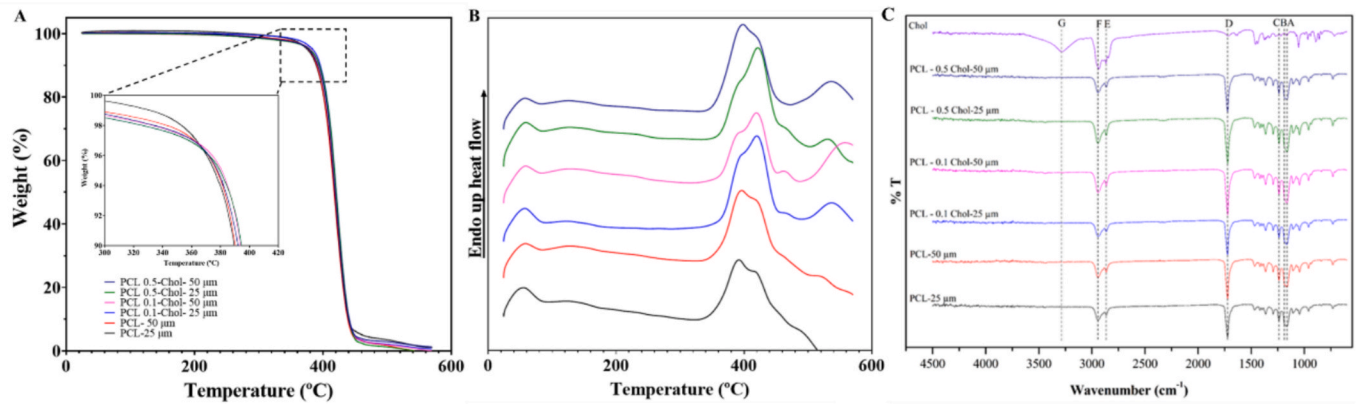

Fig. 2. (A) TGA and (B) DSC profiles of electrospun PCL and Chol-PCL meshes. (C) FTIR of the electrospun PCL meshes. Pure Chol was also used as control.

Table 3
Thermal properties of electrospun PCL and Chol–PCL meshes.

Fibers	ΔH_m (J/g)	T_m (°C)	C_x (%)	T_d (°C)
PCL- 25 µm	30.45	55.09	21.86	420.04
PCL-0.1 Chol – 25 µm	25.68	57.76	18.30	419.12
PCL-0.5 Chol – 25 µm	16.47	59.73	11.50	420.98
PCL- 50 µm	23.90	59.29	17.16	419.79
PCL-0.1 Chol – 50 µm	20.30	59.60	14.47	419.04
PCL-0.5 Chol –50 µm	17.54	58.89	12.16	397.57

polymer degradation and increases mechanical compliance, which could improve the ability of the scaffold to conform to the bone–implant interface during the early stages of healing (Cipitria et al., 2011; Dias et al., 2022).

3.3.2. FTIR-ATR

FTIR-ATR analysis confirmed the characteristic spectral features of PCL, including the C–H stretching vibrations in the 3000–2800 cm^{-1} region and the ester carbonyl (C=O) stretching band around 1750–1700 cm^{-1}, indicating that the polymer backbone remained intact after electrospinning (Tardajos et al., 2018). In electrospun meshes containing cholecalciferol, an additional broad absorption band appeared in the 3600–3200 cm^{-1} region, attributed to O–H stretching vibrations, with its intensity increasing with higher cholecalciferol content. This confirms the successful incorporation of the drug into the fibers. Moreover, no shifts were observed in the main PCL carbonyl peak, and the fingerprint region retained the typical C–O–C and C–H absorptions. Minor intensity differences between formulations likely reflect variations in dispersion rather than chemical interactions.

No additional peaks corresponding to crystalline cholecalciferol were detected, indicating uniform dispersion of the molecule within the fibers and no phase separation. Fiber thickness (25 µm vs. 50 µm) also showed no consistent spectral differences, suggesting that composition is determined by formulation rather than coating thickness (Sanhueza et al., 2023).

3.4. Mechanical properties

The tensile properties of electrospun PCL and Chol-PCL meshes were evaluated in terms of elongation at break, tensile strength, and Young's modulus (Fig. 3). Overall, mesh thickness exerted a stronger influence on mechanical behavior than cholecalciferol incorporation.

Meshes with a nominal thickness of 50 µm exhibited significantly higher ductility than their 25 µm counterparts, with elongation at break values reaching 745.89 ± 78.58% for PCL-0.5 Chol-50 µm. In contrast, thinner meshes (25 µm) displayed greater tensile strength and stiffness, with unloaded PCL-25 µm exhibiting a tensile strength of 1.39 ± 0.17 MPa and a Young's modulus of 1.90 ± 0.35 MPa. These results indicate that reduced thickness promotes tighter fiber packing and increased load transfer efficiency across the fibrous network.

Cholecalciferol incorporation led to a concentration-dependent reduction in tensile strength, particularly evident in 50 µm meshes, while simultaneously increasing elongation at break. This behavior suggests that cholecalciferol imparts a plasticizing effect within the fibrous structure, enhancing deformability but reducing resistance to fracture. Such trends are consistent with previous reports describing the incorporation of low-molecular-weight hydrophobic additives into

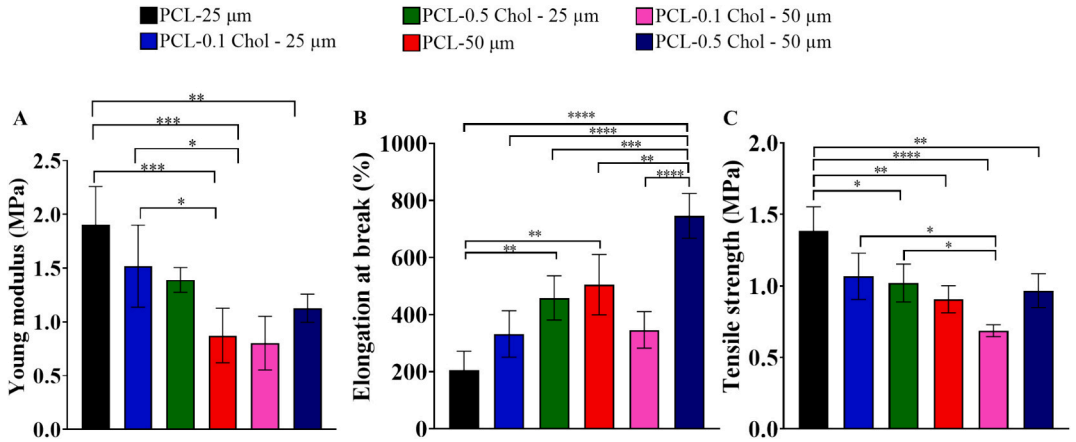

Fig. 3. Tensile properties of electrospun PCL meshes, including (A) Young's modulus, (B) elongation at break, and (C) tensile strength. Statistical differences were processed with a one-way ANOVA with Tukey's post hoc test (*$p < 0.05$, **$p < 0.01$, *** $p < 0.001$, **** $p < 0.0001$).

electrospun polymer matrices, where disruption of crystalline packing reduces ultimate strength while promoting ductility (Al-Bishari et al., 2022; Echeverria Molina et al., 2022).

Interestingly, Young's modulus showed a modest increase with cholecalciferol incorporation across formulations, despite the reduction in tensile strength. This apparent decoupling of stiffness and strength may arise from microstructural changes associated with reduced crystallinity and altered fiber–fiber interactions, as observed in the thermal analysis. Similar behavior has been reported in electrospun composite systems where localized stiffening at fiber junctions coexists with reduced global strength due to diminished lamellar continuity.

From a functional perspective, the combination of increased ductility and moderate stiffness may be advantageous for implant coatings, as compliant fibrous layers can better accommodate deformation at the bone-implant interface while maintaining sufficient mechanical integrity during early implantation and loading.

3.5. Chol release studies

The release experiments demonstrated a biphasic pattern (Fig. 4). During the first hours, the meshes released approximately 60–65% of the loaded cholecalciferol, reflecting a pronounced burst effect. This initial phase likely corresponded to drug located on or near the fiber surface, or weakly entrapped within the polymer network, and therefore readily accessible to the surrounding medium. After this rapid phase, the release rate decreased, ultimately leading to cumulative release values above 90%. As degradation advances, increased porosity and polymer chain disruption enhance matrix permeability and expose previously entrapped cholecalciferol, facilitating its release. The obtained results indicate a transition from an initially diffusion-dominated mechanism to a degradation-assisted release process at extended times (Choommongkol et al., 2022).

The drug release data were fitted to the Korsmeyer-Peppas model in order to elucidate the underlying release mechanism (Korsmeyer et al., 1983). The analysis was performed using the initial portion of the release profile ($M_t/M_\infty \leq 0.65$), excluding the burst effect at $t = 0$. The calculated release exponent was $n = 0.237$ ($R^2 = 0.837$), with a kinetic constant $k = 0.431$, according to the equation $M_t/M_\infty = 0.431\ t^{0.237}$. Since the obtained n value is lower than 0.45, the system can be classified as exhibiting Fickian diffusion-controlled release. These results indicate that drug diffusion through the matrix is the predominant mechanism governing release, while polymer relaxation or erosion plays a negligible role during the initial stages. The pronounced initial burst release suggests the presence of drug located at or near the surface of the matrix, contributing to the rapid release observed at early time points.

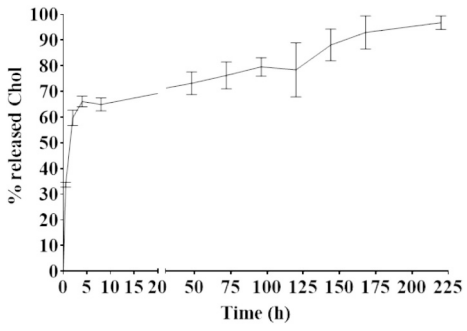

Fig. 4. Cumulative release profile (%) over time. The results showed a rapid initial release within the first hours, followed by a sustained and gradual increase over time, reaching approximately 95–100% at the latest points evaluated. Data are presented as mean ± standard deviation.

3.6. In vitro cellular response to electrospun PCL and Chol-PCL meshes

3.6.1. Cytocompatibility studies

Cell viability was evaluated using MTT assays in MSCs, MG-63 osteoblast-like cells after 1, 3, and 7 days of culture in presence of electrospun PCL and Chol-PCL meshes of different thicknesses (25 and 50 μm) in direct contact with culture media. Across all formulations and time points, cell viability remained above 70% relative to untreated controls, satisfying the criteria for non-cytotoxicity according to ISO 10993-5 (International Organization for Standardization, 2009) (Fig. 5A).

In MSC cultures, no statistically significant differences were observed between treatments at any time point (Fig. 5A), indicating that both unloaded and cholecalciferol-loaded meshes support MSC survival and metabolic activity over the experimental period. This suggests that neither cholecalciferol incorporation nor membrane thickness adversely affected MSC viability.

MG-63 cells exhibited a transient thickness-dependent response, with significantly higher viability observed at 24 h on 50 μm Chol-PCL meshes compared to 25 μm meshes (ANOVA, $p < 0.05$). However, this difference was no longer evident at 72 h or 7 days (Fig. 5A), indicating that early thickness-related effects did not persist over time.

3.6.2. Osteogenic differentiation, matrix formation, and mineralization

The osteogenic potential of electrospun meshes was further evaluated using MSCs and MG-63 cells by assessing mineralization, collagen deposition, and ALP activity after incubation in osteogenic and non-osteogenic medium. The influence of Chol concentration (0.1 and 0.5% (w/v)) and membrane thickness (25 and 50 μm) was systematically analyzed and compared with untreated controls.

Under osteogenic conditions, both MSCs and MG-63 cells cultured on all mesh-treated groups showed a marked and statistically significant increase in mineralized matrix formation compared with the control group (Fig. 5B). No statistically significant differences were detected between 0.1% and 0.5% cholecalciferol or between 25 μm and 50 μm thicknesses, indicating that the fibrous matrix itself was sufficient to enhance mineral deposition under osteogenic culture. A similar trend was observed in cells cultured in non-osteogenic medium, where significant differences were mainly found between cells cultured on the scaffolds, independently of the thickness and cholecalciferol content, compared to the control (**Fig. S3A, Supplementary Material**).

Collagen synthesis displayed time- and cell-type-dependence. In MSCs, all treated conditions exceeded controls as early as day 7, whereas MG-63 cells showed no early differences. By days 14 and 21 a similar trend was observed in cells cultured in osteogenic (Fig. 5C) and non-osteogenic conditions (**Fig. S3B, Supplementary Material**), collagen deposition was significantly higher in all mesh-treated groups for both cell lines. MSC cultures were particularly sensitive to thickness: 50 μm meshes promoted greater collagen accumulation at day 21. Although this trend appeared most visible in the 0.5 Chol-PCL group, no statistical differences were observed between drug content and thickness.

ALP increased robustly in MSCs for all mesh-treated conditions, with 50 μm meshes inducing the highest activity from day 7 and maintaining this through day 21. On MG-63 cells, ALP activity was higher on 50 μm meshes at day 7 but in the remaining timepoints all treated groups exceeded controls in both osteogenic (Fig. 5D) and non-osteogenic conditions (**Fig. S3C, Supplementary Material**).

The increases observed in ALP, collagen, and mineralization across Chol-PCL meshes are consistent with well-established Chol-mediated osteogenic signaling (Muresan et al., 2022). Previously reported in vitro studies showed that Chol promotes osteogenic differentiation, increases mineralization, and stimulates osteoblast-related markers in MSCs and osteoblast-like cells (Muresan et al., 2022; Seciu-Grama et al., 2025). Similarly, vitamin D_3 functionalization of scaffolds has similarly been shown to increase calcium deposition and osteocalcin secretion in stem cells, confirming its capacity to boost late-stage osteogenic

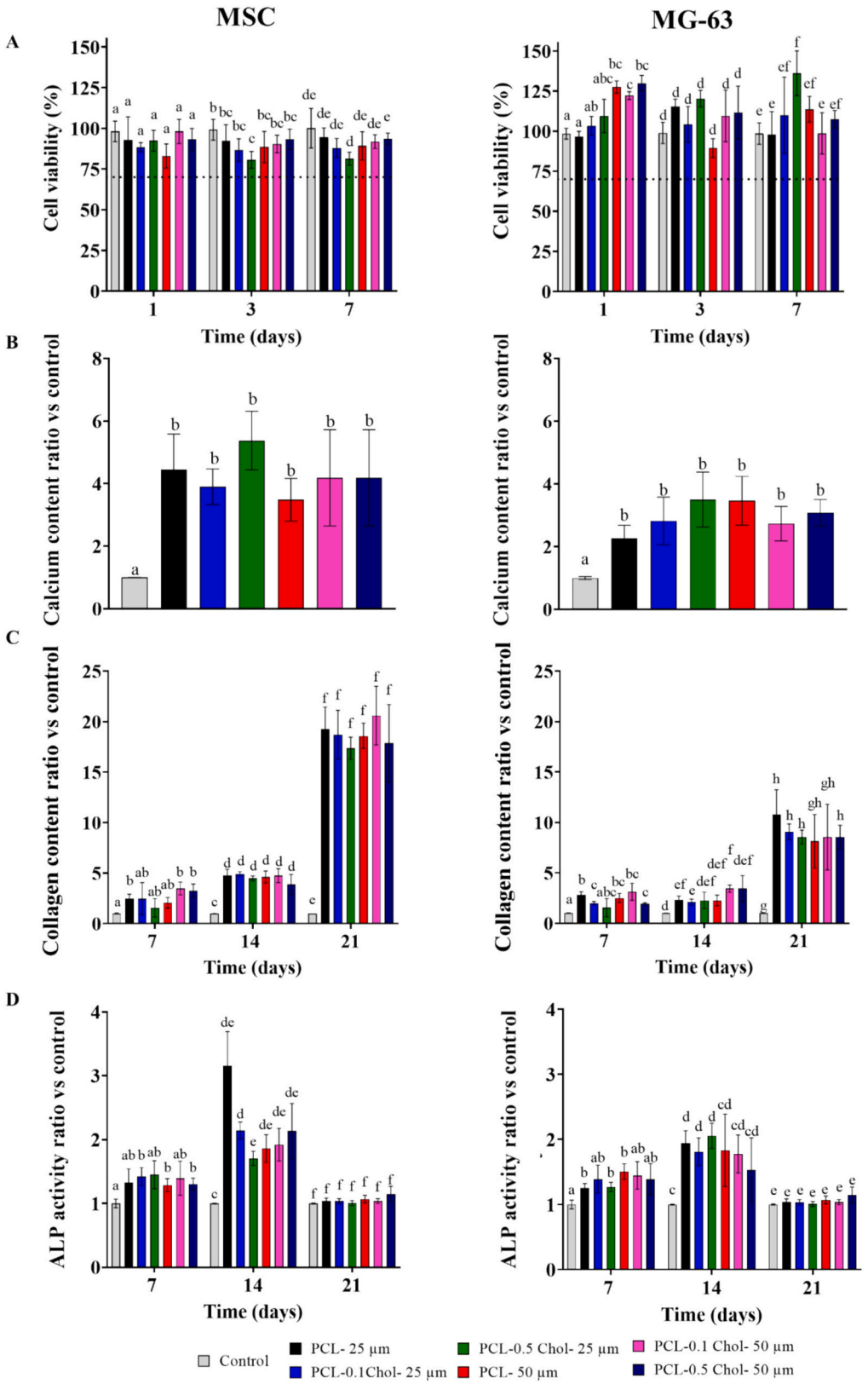

Fig. 5. (A) Cell viability of MSCs, and MG-63 cells cultured on electrospun PCL and Chol-PCL meshes (25 and 50 µm thickness) for 24 h, 72 h, and 7 days. (B) Detection of calcium in solution by Alizarin Red staining on PCL fibers non-loaded and loaded with 0.1 or 0.5% (w/v) Chol, 25 or 50 µm of thickness after 7, 14 and 21 days of incubation with MSC and MG-63 cells. (C) Detection of collagens in solution by Sirius Red staining on PCL fibers non-loaded and loaded with 0.1 or 0.5% (w/v) Chol, 25 or 50 µm of thickness after 7, 14 and 21 days of incubation with MSC and MG-63 cells. (D) Quantitative analysis of alkaline phosphatase staining on PCL fibers non-loaded and loaded with 0.1 or 0.5% (w/v) Chol, 25 or 50 µm of thickness after 7, 14 and 21 days of incubation with MSC and MG-63 cells. Data are expressed as mean ± standard deviation. Statistical differences were shown compared with non-treated cells. Statistical differences were processed with a one-way ANOVA with Tukey's post hoc test. Different letters mean statistical differences (ANOVA, $p < 0.05$).

maturation (Negut et al., 2023; Seciu-Grama et al., 2025). Furthermore, cholecalciferol-loaded polymer scaffolds have been reported to promote stronger MSC osteogenic differentiation than standard osteogenic medium alone, consistent with the ability of MSCs to metabolize cholecalciferol and respond with elevated ALP and mineral deposition (Calore et al., 2022).

3.7. *In vivo evaluation of peri-implant bone regeneration*

3.7.1. *MicroCT and histomorphometric analysis*

To investigate the osteogenic performance of Chol-loaded electrospun PCL coatings in vivo, peri-implant bone formation and bone quality were evaluated 21 days after implantation in a rat proximal tibia model. This model is widely used for assessing early, unloaded osseointegration because it provides reproducible bone healing kinetics, with peak osteoblastic activity occurring within the first three weeks, and allows standardized histological and histomorphometric evaluation of implant surface bioactivity (Scarano et al., 2024). MicroCT and BS-SEM analyses were used to assess early peri-implant bone formation after 21 days of healing. Representative BS-SEM images showed visible new bone surrounding the implant in all groups (Fig. 6A). BS-SEM histomorphometry consistently showed greater peri-implant bone area in the PCL 0.5-Chol-25 μm compared with controls and PCL 0.5-Chol- 50 μm coatings, reflecting improved early bone infill at the interface between the implant and the surrounding tissue.

MicroCT analysis showed significantly higher BV/TV in the PCL 0.5-Chol-25 μm group (21.43 ± 6.76%) compared with uncoated implants (11.76 ± 2.76%) and with the PCL 0.5-Chol-50 μm coatings (14.74 ± 4.34%). Trabecular thickness was also higher in the PCL 0.5-Chol- 25 μm group relative to controls and comparable to values typically observed in early healing (Fang et al., 2014). Trabecular separation and total porosity were lowest in the PCL 0.5-Chol- 25 μm coating group, indicating a denser and more interconnected trabecular network at the implant interface (Fig. 6B). Therefore, the higher trabecular thickness observed in the PCL 0.5-Chol- 25 μm group indicates not only increased bone quantity but also improved structural quality. The absence of significant differences between both coated groups in this parameter suggests that coating presence itself enhanced trabecular maturation, although only the PCL 0.5-Chol- 25 μm thickness translated this effect into a significantly greater overall bone volume.

Trabecular separation was significantly lower in the PCL 0.5-Chol-25 μm group (138.29 ± 8.13) compared to both the control (150.97 ± 4.83) and the PCL 0.5-Chol-50 μm coating group (150.24 ± 7.26). Reduced trabecular separation indicates a more compact and interconnected trabecular network (Meller et al., 2022). In physiological trabecular bone, trabecular values typically range approximately between 150 and 300 μm, depending on species, anatomical location, and age (Guo et al., 2010). The values observed in the PCL 0.5-Chol- 25 μm group fall within this physiological range but are closer to the lower end compared to the other groups, suggesting a denser and potentially more

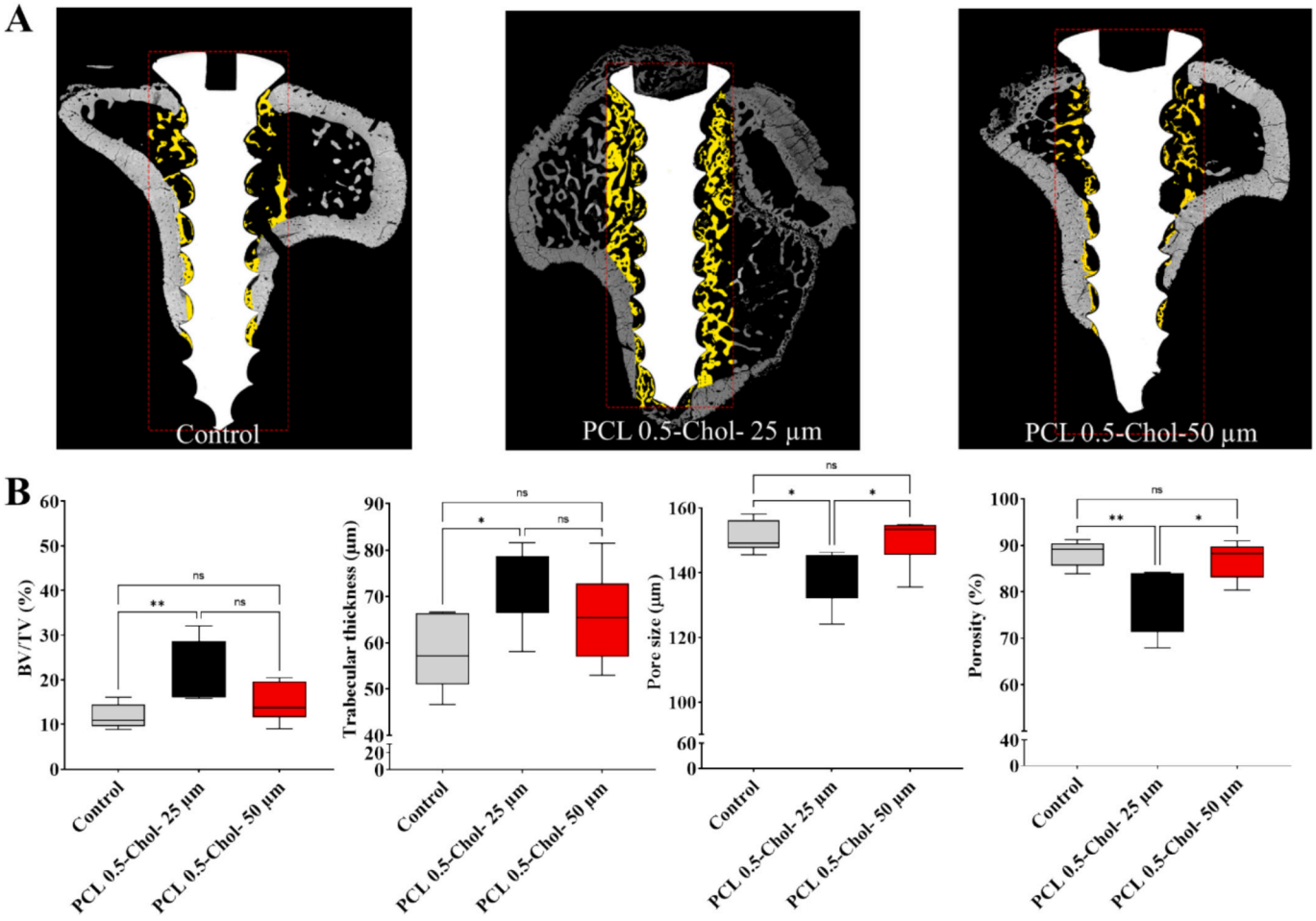

Fig. 6. (A) Representative microphotographs obtained by BS-SEM of resin-embedded bone sections. Newly formed bone is highlighted in yellow to facilitate visualization and quantification. (B) Quantitative results of bone regeneration measured using micro-CT in bone defects treated with Ti mini-implant coated with 0.5% (w/v) Chol-PCL nanofibers (25 μm thickness), and Ti mini-implant coated with 0.5% w/v Chol-PCL nanofibers (50 μm thickness). Samples from PCL-0.5 Chol-25 μm-coated group exhibited the most extensive bone formation adjacent to the implant surface, showing a statistically significant difference compared to control group ($p < 0.05$).

mechanically robust architecture. From a regenerative standpoint, reduced trabecular separation is advantageous, as it reflects enhanced structural continuity and improved load distribution capacity.

Consistent with these findings, total porosity was significantly lower in the PCL 0.5-Chol- 25 μm coating group (78.55 ± 6.75) compared to the control (88.23 ± 2.76) and the PCL 0.5-Chol- 50 μm coating group (86.70 ± 3.78). Trabecular bone porosity under physiological conditions typically ranges between approximately 50% and 90%, depending on anatomical site and metabolic status (Dziaduszewska & Zieliński, 2021). The porosity value observed in the PCL 0.5-Chol-25 μm group remains within the normal physiological range but is markedly reduced relative to the other groups, indicating a higher fraction of mineralized tissue within the analyzed volume.

These results align with previous evidence showing that vitamin D_3-functionalized implant surfaces enhance trabecular microarchitecture and bone repair in vivo. Using a similar animal model, Chol coatings increased bone volume, reduced porosity, and improved trabecular organization around implants, demonstrating that local delivery can accelerate early peri-implant bone maturation (Pitol-Palin et al., 2025).

As observed, Chol-PCL coating created a more favorable microenvironment for early peri-implant bone formation, generating higher bone volume and a denser trabecular structure than the thicker coating. Similar improvements in trabecular organization and *peri*-implant bone quality have been reported for vitamin D_3-functionalized implant surfaces *in vivo*, supporting the idea that localized delivery of vitamin D_3 can enhance early bone maturation around titanium implants (Szwed-Georgiou et al., 2023; Thibault et al., 2010; Werny et al., 2022; Zhang et al., 2025).

The more extensive bone formation observed adjacent to implants coated with PCL 0.5-Chol-25 μm may be attributed, at least in part, to thickness-dependent mechanical stability. Consistent with these findings, nanofibrous coatings exceeding 50–75 μm have been reported to be at increased risk of delamination and cracking due to reduced interfacial toughness under implantation-related shear forces (Shakil & Hájek, 2026; Vera-Becerra et al., 2026).

3.7.2. Toxicological assessment

Serum biochemical markers and histological analyses were used to assess potential systemic or local adverse effects associated with the Chol-PCL coatings. Overall, the results indicated no evidence of systemic toxicity. Although creatinine and uric acid showed mild differences between groups (**Fig. S4**, **Supplementary material**), all values remained within physiological ranges for healthy rats, and no alterations suggestive of renal or hepatic dysfunction were observed. Similarly, liver enzymes and mineral metabolism markers (ALT, AST, ALP, calcium, phosphorus, albumin) showed no significant deviations, indicating that neither the polymer coatings nor the locally delivered cholecalciferol produced measurable systemic stress (Al-Bishari et al., 2022; Alemáan et al., 1998; El-Shenawy et al., 2012; León Goñi et al., 2011; Sitar et al., 2024).

Histologically, hepatic and renal tissues (**Fig. S5 and S6**, **Table S2 and Table S3**, **Supplementary material**) showed preserved architecture across all groups, with only mild events, such as vascular congestion, discrete inflammatory infiltrates, or minimal hepatocyte alterations, consistent with normal postoperative or metabolic variation rather than material-induced injury (Aksoy et al., 2024; Badawi, 2019; Hamdi et al., 2019). Liver sections occasionally displayed mild congestion, scattered binucleated hepatocytes, or isolated lipid vacuoles, but no necrosis, apoptosis, or fibrotic remodeling was detected. Renal morphology was similarly preserved, with occasional focal congestion or glomerular atrophy not differing between coated and uncoated groups and lacking features of tubular necrosis or interstitial fibrosis. Semi-quantitative scoring confirmed the absence of coating-related pathology, as lesion grades were low and distributed similarly across experimental groups, aligning with reports indicating that short-term exposure to bioactive polymeric systems does not compromise renal microarchitecture (Hamdi et al., 2019).

The obtained results evidenced that PCL-Chol coatings on Ti mini-implants were biocompatible, eliciting only minimal physiological responses and no detectable systemic burden. The absence of material-related toxicity is consistent with previous evidence showing that Chol-functionalized implant surfaces support bone repair without compromising biochemical or histological homeostasis in vivo. This supports the overall safety of the coating strategy and reinforces the suitability of thin Chol-PCL layers for applications requiring localized osteoactive delivery without systemic side effects. Future studies will investigate the *in vivo* osseointegration of the coated implants in a Goto-Kakizaki type 2 diabetic rat model, providing further validation of their performance under metabolically compromised conditions and strengthening the translational relevance of this approach.

4. Conclusions

Cholecalciferol-loaded PCL coatings were successfully fabricated using electrospinning, resulting in uniform and homogeneous nanofibrous structures with controlled cholecalciferol release. *In vitro*, the coatings were cytocompatible and enhanced osteogenic activity in bone regeneration relevant cell lines, increasing ALP activity, collagen synthesis, and mineralized ECM deposition. *In vivo*, Chol-PCL coating on Ti mini implants significantly improved early peri-implant bone formation, with higher bone volume and a denser trabecular structure at the implant-bone interface without inducing systemic or local toxicity. These results demonstrate that cholecalciferol-releasing nanofiber coatings might offer a safe and effective strategy to modulate the peri-implant microenvironment and accelerate early osseointegration.

Declaration of generative AI use

During the preparation of this work, the authors used generative AI solely to assist with proofreading and improving the English translation of selected paragraphs. After using this tool, the authors reviewed and edited the content as needed and take full responsibility for the content of the publication.

CRediT authorship contribution statement

Francisca Acevedo: Writing – review & editing, Writing – original draft, Visualization, Supervision, Resources, Project administration, Funding acquisition, Conceptualization. **Jeyson Hermosilla:** Writing – original draft, Methodology, Investigation, Formal analysis, Data curation. **Alexis Vera:** Writing – original draft, Methodology, Investigation, Formal analysis, Data curation. **Felipe Galvez-Jirón:** Writing – original draft, Methodology, Investigation, Formal analysis, Data curation. **Vanessa Campos-Bijit:** Methodology. **Rodrigo Navia:** Writing – review & editing, Visualization, Funding acquisition. **Nicolas Cohn:** Methodology. **Pablo Navarro:** Formal analysis, Data curation. **Pablo Acuña-Mardones:** Methodology, Investigation, Formal analysis, Data curation. **Víctor Beltrán:** Writing – review & editing, Writing – original draft, Formal analysis, Conceptualization. **Luis Diaz-Gomez:** Writing – review & editing, Data curation. **Maria Pita-Vilar:** Writing – review & editing, Data curation. **Iván Valdivia-Gandur:** Writing – review & editing, Supervision, Methodology, Investigation, Formal analysis, Data curation, Conceptualization. **María Cristina Manzanares:** Writing – review & editing.

Declaration of competing interest

The authors declare that they have no known competing financial interests or personal relationships that could have appeared to influence the work reported in this paper.

Acknowledgments

This work was supported by Agencia Nacional de Investigación y Desarrollo de Chile (ANID), ANID-FONDECYT project N°1230544 and ANID-Milenio-NCN2023_054. This work was partially done by Dr. Iván Valdivia Gandur into visit at the Universitat de Barcelona supported by MINEDUC-UA project, code ANT 22991, and by Universidad de La Frontera, PP24-0019 support. Rodrigo Navia acknowledges the support of ANID CA2FST CIN250015. Maria Pita-Vilar acknowledges Xunta de Galicia for the predoctoral contract ED481A-2023-164. The authors gratefully acknowledge Dr. Bernardo Venegas (Stomatology Department, Faculty of Dentistry, Universidad de Talca, Chile) for his valuable contribution to the toxicological analysis conducted in this study.

Appendix A. Supplementary data

Supplementary data to this article can be found online at https://doi.org/10.1016/j.ijpharm.2026.126874.

Data availability

Data will be made available on request.

References

Abd-Elaziem, W., Darwish, M.A., Hamada, A., Daoush, W.M., 2024. Titanium-based alloys and composites for orthopedic implants applications: a comprehensive review. Mater. Des. 241, 112850. https://doi.org/10.1016/j.matdes.2024.112850.

Agarwal, R., García, A.J., 2015. Biomaterial strategies for engineering implants for enhanced osseointegration and bone repair. Adv. Drug Deliv. Rev. 94, 53–62. https://doi.org/10.1016/j.addr.2015.03.013.

Aksoy, S., Kuloğlu, N., Karabulut, D., Yakan, B., 2024. Investigation of the effect of Myricetin on Cisplatin-induced liver hepatotoxicity. Rev. Assoc. Méd. Brasileira 70 (7). https://doi.org/10.1590/1806-9282.20240136.

Al-Bishari, A.M., Al-Shaaobi, B.A., Al-Bishari, A.A., Al-Baadani, M.A., Yu, L., Shen, J., Cai, L., Shen, Y., Deng, Z., Gao, P., 2022. Vitamin D and curcumin-loaded PCL nanofibrous for engineering osteogenesis and immunomodulatory scaffold. Front. Bioeng. Biotechnol. 10. https://doi.org/10.3389/fbioe.2022.975431.

Alemáan, C.L., Más, R.M., Rodeiro, I., Noa, M., Hernández, C., Menéndez, R., Gámez, R., 1998. Reference database of the main physiological parameters in Sprague-Dawley rats from 6 to 32 months. Lab. Anim 32 (4), 457–466. https://doi.org/10.1258/002367798780599802.

Anjum, S., Rahman, F., Pandey, P., Arya, D.K., Alam, M., Rajinikanth, P.S., Ao, Q., 2022. Electrospun biomimetic nanofibrous scaffolds: a promising prospect for bone tissue engineering and regenerative medicine. Int. J. Mol. Sci. 23 (16), 9206. https://doi.org/10.3390/ijms23169206.

Badawi, M.S., 2019. Histological study of the protective role of ginger on piroxicam-induced liver toxicity in mice. J. Chin. Med. Assoc. 82 (1), 11–18. https://doi.org/10.1016/j.jcma.2018.06.006.

Belgheisi, G., Nazarpak, M.H., Hashjin, M.S., 2020. Bone tissue engineering electrospun scaffolds based on layered double hydroxides with the ability to release vitamin D3: fabrication, characterization and in vitro study. Appl. Clay Sci. 185, 105434. https://doi.org/10.1016/j.clay.2019.105434.

Beltrán, V., Acevedo, F., Valdivia Gandur, I., Sanhueza, C., & Venegas, B. (2023). *Bilayer membrane that promotes bone regeneration and prevents post-operative complications*. World Intellectual Property Organization (WIPO). https://patentscope.wipo.int/search/es/WO2024138282.

Beltrán, V., Weber, B., Lillo, R., Manzanares, M.-C., Sanzana, C., Fuentes, N., Acuña-Mardones, P., Valdivia-Gandur, I., 2020. Histomorphometric analysis of osseointegrated grade v titanium mini transitional implants in edentulous mandible by backscattered scanning electron microscopy (BS-SEM). Metals 11 (1), 2. https://doi.org/10.3390/met11010002.

Bohara, S., Suthakorn, J., 2022. Surface coating of orthopedic implant to enhance the osseointegration and reduction of bacterial colonization: a review. Biomater. Res. 26 (1). https://doi.org/10.1186/s40824-022-00269-3.

Cai, J., Xiong, Z., Zhou, M., Tan, J., Zeng, F., MeihuMa, L., Xiong, H., 2014. Thermal properties and crystallization behavior of thermoplastic starch/poly(ε-caprolactone) composites. Carbohydr. Polym. 102, 746–754. https://doi.org/10.1016/j.carbpol.2013.10.095.

Calore, A.R., Hadavi, D., Honing, M., Albillos-Sanchez, A., Mota, C., Bernaerts, K., Harings, J., Moroni, L., 2022. Cholecalciferol as bioactive plasticizer of high molecular weight Poly(D,L-Lactic Acid) scaffolds for bone regeneration. Tissue Eng. Part C Methods 28 (7), 335–350. https://doi.org/10.1089/ten.tec.2022.0041.

Chen, Q., Gu, J., Zhang, H., Zhang, D., Wang, Y., Liu, G., Zhu, X., Zhang, X., Cao, C., Yuan, Y., Liu, R., 2025. Promoting implant osseointegration via the osteoblast-selective β-amino acid polymer strategy. Nat. Commun. 16 (1), 7190. https://doi.org/10.1038/s41467-025-58394-1.

Cheng, H., Chawla, A., Yang, Y., Li, Y., Zhang, J., Jang, H.L., Khademhosseini, A., 2017. Development of nanomaterials for bone-targeted drug delivery. Drug Discov. Today 22 (9), 1336–1350. https://doi.org/10.1016/j.drudis.2017.04.021.

Choommongkol, V., Ruangsuriya, J., Suttiarporn, P., Punyodom, W., Thapsukhon, B., 2022. Polyester-releasing sesamin by electrospinning technique for the application of bone tissue engineering. Des. Monomers Polym. 25 (1), 231–244. https://doi.org/10.1080/15685551.2022.2111857.

Christakos, S., Dhawan, P., Verstuyf, A., Verlinden, L., Carmeliet, G., 2016. Vitamin D: Metabolism, Molecular Mechanism of Action, and Pleiotropic Effects. Physiol. Rev. 96 (1), 365–408. https://doi.org/10.1152/physrev.00014.2015.

Cipitria, A., Skelton, A., Dargaville, T.R., Dalton, P.D., Hutmacher, D.W., 2011. Design, fabrication and characterization of PCL electrospun scaffolds—a review. J. Mater. Chem. 21 (26), 9419. https://doi.org/10.1039/c0jm04502k.

Coelho, P.G., Jimbo, R., Tovar, N., Bonfante, E.A., 2015. Osseointegration: Hierarchical designing encompassing the macrometer, micrometer, and nanometer length scales. Dent. Mater. 31 (1), 37–52. https://doi.org/10.1016/j.dental.2014.10.007.

Colnot, C., Romero, D.M., Huang, S., Rahman, J., Currey, J.A., Nanci, A., Brunski, J.B., Helms, J.A., 2007. Molecular analysis of healing at a bone-implant interface. J. Dent. Res. 86 (9), 862–867. https://doi.org/10.1177/154405910708600911.

da Silva, T.B.V., de Oliveira, A., Moreira, T.F.M., da Silva, K.C., Zanin, R.C., Bona, E., Gonçalves, O.H., Shirai, M.A., Peron, A.P., Leimann, F.V., 2021. Analytical validation of an ultraviolet–visible procedure for determining vitamin D3 in vitamin D3-loaded microparticles and toxigenetic studies for incorporation into food. Food Chem. 360, 129979. https://doi.org/10.1016/j.foodchem.2021.129979.

Das, S., Dholam, K., Gurav, S., Bendale, K., Ingle, A., Mohanty, B., Chaudhari, P., Bellare, J.R., 2019. Accentuated osseointegration in osteogenic nanofibrous coated titanium implants. Sci. Rep. 9 (1), 17638. https://doi.org/10.1038/s41598-019-53884-x.

Das, S., Gurav, S., Soni, V., Ingle, A., Mohanty, B.S., Chaudhari, P., Bendale, K., Dholam, K., Bellare, J.R., 2018. Osteogenic nanofibrous coated titanium implant results in enhanced osseointegration: in vivo preliminary study in a rabbit model. Tissue Eng. Regener. Med. 15 (2), 231–247. https://doi.org/10.1007/s13770-017-0106-6.

Dias, J.R., Sousa, A., Augusto, A., Bártolo, P.J., Granja, P.L., 2022. Electrospun polycaprolactone (PCL) degradation: an in vitro and in vivo study. Polymers 14 (16), 3397. https://doi.org/10.3390/polym14163397.

Dieterle, M.P., Steinberg, T., Tomakidi, P., Nohava, J., Vach, K., Schulz, S.D., Hellwig, E., Proksch, S., 2022. Novel in situ-cross-linked electrospun gelatin/hydroxyapatite nonwoven scaffolds prove suitable for periodontal tissue engineering. Pharmaceutics 14 (6), 1286. https://doi.org/10.3390/pharmaceutics14061286.

Ding, Y., Li, W., Zhang, F., Liu, Z., Zanjanizadeh Ezazi, N., Liu, D., Santos, H.A., 2019. Electrospun fibrous architectures for drug delivery, tissue engineering and cancer therapy. Adv. Funct. Mater. 29 (2). https://doi.org/10.1002/adfm.201802852.

Dohan Ehrenfest, D.M., Coelho, P.G., Kang, B.-S., Sul, Y.-T., Albrektsson, T., 2010. Classification of osseointegrated implant surfaces: materials, chemistry and topography. Trends Biotechnol. 28 (4), 198–206. https://doi.org/10.1016/j.tibtech.2009.12.003.

Douglas, P., Kuhs, M., Sajjia, M., Khraisheh, M., Walker, G., Collins, M.N., Albadarin, A. B., 2016. Bioactive PCL matrices with a range of structural & rheological properties. React. Funct. Polym. 101, 54–62. https://doi.org/10.1016/j.reactfunctpolym.2016.02.004.

Dumitriu, R.P., Stoleru, E., Mitchell, G.R., Vasile, C., Brebu, M., 2021. Bioactive electrospun fibers of poly(ε-caprolactone) incorporating α-tocopherol for food packaging applications. Molecules 26 (18), 5498. https://doi.org/10.3390/molecules26185498.

Dziaduszewska, M., Zieliński, A., 2021. Structural and material determinants influencing the behavior of porous ti and its alloys made by additive manufacturing techniques for biomedical applications. Materials 14 (4), 712. https://doi.org/10.3390/ma14040712.

Echeverria Molina, M.I., Chen, C.-A., Martinez, J., Tran, P., Komvopoulos, K., 2022. Novel electrospun polycaprolactone/calcium alginate scaffolds for skin tissue engineering. Materials 16 (1), 136. https://doi.org/10.3390/ma16010136.

El-Shenawy, N.S., Mohsen, Q., Fadl-allah, S.A., 2012. Oxidative stress and antioxidant responses of liver and kidney tissue after implantation of titanium or titanium oxide coated plate in rat tibiae. J. Mater. Sci. - Mater. Med. 23 (7), 1763–1774. https://doi.org/10.1007/s10856-012-4648-9.

Fang, L., Ding, X., Wang, H., Zhu, X.-H., 2014. Chronological changes in the microstructure of bone during peri-implant healing: a microcomputed tomographic evaluation. Br. J. Oral Maxillofac. Surg. 52 (9), 816–821. https://doi.org/10.1016/j.bjoms.2014.07.097.

García-de-Albeniz, N., Jiménez-Piqué, E., Roa, J.J., Mas-Moruno, C., 2023. A review of surface topographical modification strategies of 3Y-TZP: effect in the physicochemical properties, microstructure, mechanical reliability, and biological response. J. Eur. Ceram. Soc. 43 (8), 2977–3004. https://doi.org/10.1016/j.jeurceramsoc.2023.02.043.

Gedik, B., Erdem, M.A., 2025. Electrospun PCL membranes for localized drug delivery and bone regeneration. BMC Biotech. 25 (1), 31. https://doi.org/10.1186/s12896-025-00965-7.

Geetha, M., Singh, A.K., Asokamani, R., Gogia, A.K., 2009. Ti based biomaterials, the ultimate choice for orthopaedic implants – a review. Prog. Mater Sci. 54 (3), 397–425. https://doi.org/10.1016/j.pmatsci.2008.06.004.

Golpour, A., Bereswill, S., Heimesaat, M.M., 2019. Antimicrobial and immune-modulatory effects of vitamin D provide promising antibiotics-independent approaches to tackle bacterial infections – lessons learnt from a literature survey. European Journal of Microbiology and Immunology 9 (3), 80–87. https://doi.org/10.1556/1886.2019.00014.

Gregory, C.A., Grady Gunn, W., Peister, A., Prockop, D.J., 2004. An Alizarin red-based assay of mineralization by adherent cells in culture: comparison with cetylpyridinium chloride extraction. Anal. Biochem. 329 (1), 77–84. https://doi.org/10.1016/j.ab.2004.02.002.

Guo, J., Liu, M., Yang, D., Bouxsein, M.L., Thomas, C.C., Schipani, E., Bringhurst, F.R., Kronenberg, H.M., 2010. Phospholipase C signaling via the parathyroid hormone (PTH)/PTH-related peptide receptor is essential for normal bone responses to PTH. Endocrinology 151 (8), 3502–3513. https://doi.org/10.1210/en.2009-1494.

Hamdi, H., Othmène, Y.B., Ammar, O., Klifi, A., Hallara, E., Ghali, F.B., Houas, Z., Najjar, M.F., Abid-Essefi, S., 2019. Oxidative stress, genotoxicity, biochemical and histopathological modifications induced by epoxiconazole in liver and kidney of Wistar rats. Environ. Sci. Pollut. Res. 26 (17), 17535–17547. https://doi.org/10.1007/s11356-019-05022-3.

Hussain, B., Grytten, J.I., Rongen, G., Sanz, M., Haugen, H.J., 2024. Surface topography has less influence on peri-implantitis than patient factors: a comparative clinical study of two dental implant systems. ACS Biomater Sci. Eng. 10 (7), 4562–4574. https://doi.org/10.1021/acsbiomaterials.3c01809.

International Organization for Standardization. (2009). *ISO 10993-5:2009. Biological evaluation of medical devices — Part 5: Tests for in vitro cytotoxicity*. International Organization for Standardization.

Jeon, H., Lee, H., Kim, G., 2014. A surface-modified poly(ε-caprolactone) scaffold comprising variable nanosized surface-roughness using a plasma treatment. Tissue Eng. Part C Methods 20 (12), 951–963. https://doi.org/10.1089/ten.tec.2013.0701.

Jo, Y., Majumdar, U., Bose, S., 2024. Vitamin D3 release from MgO doped 3D printed TCP scaffolds for bone regeneration. ACS Biomater Sci. Eng. 10 (3), 1676–1685. https://doi.org/10.1021/acsbiomaterials.3c01779.

Korsmeyer, R.W., Gurny, R., Doelker, E., Buri, P., Peppas, N.A., 1983. Mechanisms of solute release from porous hydrophilic polymers. Int. J. Pharm. 15 (1), 25–35. https://doi.org/10.1016/0378-5173(83)90064-9.

Langenbach, F., Handschel, J., 2013. Effects of dexamethasone, ascorbic acid and β-glycerophosphate on the osteogenic differentiation of stem cells in vitro. Stem Cell Res Ther 4 (5), 117. https://doi.org/10.1186/scrt328.

León Goñi, A. C., Blanco, D., Peña, A., Ronda, M., González, B. O., Arteaga, M. E., Bada, A. M., González, Y., & Mancebo, A. (2011). Valores hematológicos y bioquímicos de las ratas Sprague Dawley producidas en CENPALAB, Cenp: SPRD. *REDVET. Revista Electrónica de Veterinaria*, *12*(11), 1–10. http://www.veterinaria.org/revistas/redvet/n111111/111101.pdf.

Meller, S.N., de Oliveira, M.C., Krueger, G.F., Younan, K.Z., Gassen, H.T., Hernández, P. A.G., Moure, S.P., Miguens, S.A.Q., 2022. Micro-CT analysis of the mandibular bone microarchitecture of rats after radiotherapy and low-power laser therapy. Lasers Med. Sci. 37 (6), 2645–2653. https://doi.org/10.1007/s10103-022-03532-0.

Miron, R.J., Estrin, N.E., Paz, A., Gruber, R., Farshidfar, N., Zhang, Y., Sculean, A., Wiedemann, T.G., Ahmad, P., 2025. Relationship between vitamin D deficiency and early implant failure and osseointegration. Periodontology 2000. https://doi.org/10.1111/prd.70017.

Muresan, G., Hedesiu, M., Lucaciu, O., Boca, S., Petrescu, N., 2022. Effect of vitamin D on bone regeneration: a review. Medicina 58 (10), 1337. https://doi.org/10.3390/medicina58101337.

Negut, I., Gradisteanu-Pircalabioru, G., Dinu, M., Bita, B., Parau, A.C., Grumezescu, V., Ristoscu, C., Chifiriuc, M.C., 2023. Bioglass and vitamin D3 coatings for titanium implants: osseointegration and corrosion protection. Biomedicines 11 (10), 2772. https://doi.org/10.3390/biomedicines11102772.

Nhlapo, N., Dzogbewu, T.C., de Smidt, O., 2022. Nanofiber polymers for coating titanium-based biomedical implants. Fibers 10 (4), 36. https://doi.org/10.3390/fib10040036.

Palmquist, A., Omar, O.M., Esposito, M., Lausmaa, J., Thomsen, P., 2010. Titanium oral implants: surface characteristics, interface biology and clinical outcome. J. R. Soc. Interface 7 (suppl_5). https://doi.org/10.1098/rsif.2010.0118.focus.

Pandey, C., Rokaya, D., Bhattarai, B.P., 2022. Contemporary concepts in osseointegration of dental implants: a review. Biomed Res. Int. 2022 (1). https://doi.org/10.1155/2022/6170452.

Paxton, N.C., Allenby, M.C., Lewis, P.M., Woodruff, M.A., 2019. Biomedical applications of polyethylene. Eur. Polym. J. 118, 412–428. https://doi.org/10.1016/j.eurpolymj.2019.05.037.

Pereira, I.H.L., Ayres, E., Averous, L., Schlatter, G., Hebraud, A., de Paula, A.C.C., Viana, P.H.L., Goes, A.M., Oréfice, R.L., 2014. Differentiation of human adipose-derived stem cells seeded on mineralized electrospun co-axial poly(ε-caprolactone) (PCL)/gelatin nanofibers. J. Mater. Sci. - Mater. Med. 25 (4), 1137–1148. https://doi.org/10.1007/s10856-013-5133-9.

Pitol-Palin, L., Sousa, I.C., de Araújo, J.C.R., de Souza Batista, F.R., Inoue, B.K.N., Botacin, P.R., de Vasconcellos, L.M.R., Lisboa-Filho, P.N., Okamoto, R., 2025. Vitamin D3-coated surfaces and their role in bone repair and peri-implant biomechanics. Biology 14 (5), 476. https://doi.org/10.3390/biology14050476.

Sanhueza, C., Hermosilla, J., Klein, C., Chaparro, A., Valdivia-Gandur, I., Beltrán, V., Acevedo, F., 2023. Osteoinductive electrospun scaffold based on PCL-col as a regenerative therapy for peri-implantitis. Pharmaceutics 15 (7), 1939. https://doi.org/10.3390/pharmaceutics15071939.

Scarano, A., Khater, A.G.A., Gehrke, S.A., Inchingolo, F., Tari, S.R., 2024. Animal models for investigating osseointegration: an overview of implant research over the last three decades. J. Funct. Biomater. 15 (4), 83. https://doi.org/10.3390/jfb15040083.

Schulze, M., Jäger, M., Schubert, U.S., 2012. Poly(ϵ-caprolactone) decorated with one room-temperature red-emitting ruthenium(II) complex: synthesis, characterization, thermal and optical properties. Macromol. Rapid Commun. 33 (6–7), 579–584. https://doi.org/10.1002/marc.201100783.

Seciu-Grama, A.-M., Lazăr, S.E., Petrescu, S., Mocioiu, O.C., Crăciunescu, O., Atkinson, I., 2025. Impact of vitamin D3 functionalization on the osteogenic capacity of bioinspired 3D scaffolds based on Ce-doped bioactive glass and spongia agaricina. J. Funct. Biomater. 16 (4), 141. https://doi.org/10.3390/jfb16040141.

Sitar, M.E., Donmez Cakil, Y., Ipek, B.O., Altıner, N., Aydin, M.S., Gunal, H., Atamis, A. D., Karadeniz, A., 2024. Experimental vitamin D deficiency in rats: clinical chemistry, histopathological, and immunological evaluation. Cureus. https://doi.org/10.7759/cureus.67490.

Smeets, R., Stadlinger, B., Schwarz, F., Beck-Broichsitter, B., Jung, O., Precht, C., Kloss, F., Gröbe, A., Heiland, M., Ebker, T., 2016. Impact of dental implant surface modifications on osseointegration. Biomed Res. Int. 2016, 1–16. https://doi.org/10.1155/2016/6285620.

Song, W., Seta, J., Chen, L., Bergum, C., Zhou, Z., Kanneganti, P., Kast, R.E., Auner, G.W., Shen, M., Markel, D.C., Ren, W., Yu, X., 2017. Doxycycline-loaded coaxial nanofiber coating of titanium implants enhances osseointegration and inhibits *Staphylococcus aureus* infection. Biomed. Mater. 12 (4), 045008. https://doi.org/10.1088/1748-605X/aa6a26.

Szwed-Georgiou, A., Płociński, P., Kupikowska-Stobba, B., Urbaniak, M.M., Rusek-Wala, P., Szustakiewicz, K., Piszko, P., Krupa, A., Biernat, M., Gazińska, M., Kasprzak, M., Nawrotek, K., Mira, N.P., Rudnicka, K., 2023. Bioactive materials for bone regeneration: biomolecules and delivery systems. ACS Biomater Sci. Eng. 9 (9), 5222–5254. https://doi.org/10.1021/acsbiomaterials.3c00609.

Talebian, S., Mendes, B., Conniot, J., Farajikhah, S., Dehghani, F., Li, Z., Bitoque, D., Silva, G., Naficy, S., Conde, J., Wallace, G.G., 2023. Biopolymeric coatings for local release of therapeutics from biomedical implants. Adv. Sci. 10 (12). https://doi.org/10.1002/advs.202207603.

Tardajos, M.G., Cama, G., Dash, M., Misseeuw, L., Gheysens, T., Gorzelanny, C., Coenye, T., Dubruel, P., 2018. Chitosan functionalized poly-ε-caprolactone electrospun fibers and 3D printed scaffolds as antibacterial materials for tissue engineering applications. Carbohydr. Polym. 191, 127–135. https://doi.org/10.1016/j.carbpol.2018.02.060.

Thibault, R.A., Scott Baggett, L., Mikos, A.G., Kasper, F.K., 2010. Osteogenic differentiation of mesenchymal stem cells on pregenerated extracellular matrix scaffolds in the absence of osteogenic cell culture supplements. Tissue Eng. A 16 (2), 431–440. https://doi.org/10.1089/ten.tea.2009.0583.

Shakil, U.A., Hájek, P., 2026. Electrospun nanofibres for load-bearing composite materials—a review of techniques, mechanical properties and durability. Polymer Comp. 47 (5), 3917–3945. https://doi.org/10.1002/pc.70714.

Sharp, P.E., Villano, J.S., 2012. The Laboratory Rat, 2nd ed. CRC Press.

Valdivia-Gandur, I., Engelke, W., Beltrán, V., Borie, E., Fuentes, R., Manzanares-Céspedes, M.C., 2016. Novel use of cranial epidural space in rabbits as an animal model to investigate bone volume augmentation potential of different bone graft substitutes. Head Face Med. 12 (1), 35. https://doi.org/10.1186/s13005-016-0131-z.

Vera-Becerra, A., Valdivia-Gandur, I., Acuña-Mardones, P., Acevedo, F., Veuthey, C., Beltrán, V., 2026. Refined surgical protocol for the insertion of bioactive-coated titanium microscrews in the rat tibia. In Vivo 40 (1), 159–169. https://doi.org/10.21873/invivo.14181.

Walsh, B.J., Thornton, S.C., Penny, R., Breit, S.N., 1992. Microplate reader-based quantitation of collagens. Anal. Biochem. 203 (2), 187–190. https://doi.org/10.1016/0003-2697(92)90301-M.

Wang, X., Xu, S., Zhou, S., Xu, W., Leary, M., Choong, P., Qian, M., Brandt, M., Xie, Y.M., 2016. Topological design and additive manufacturing of porous metals for bone scaffolds and orthopaedic implants: a review. Biomaterials 83, 127–141. https://doi.org/10.1016/j.biomaterials.2016.01.012.

Werny, J.G., Sagheb, K., Diaz, L., Kämmerer, P.W., Al-Nawas, B., Schiegnitz, E., 2022. Does vitamin D have an effect on osseointegration of dental implants? a systematic review. Int. J. Implant Dent. 8 (1), 16. https://doi.org/10.1186/s40729-022-00414-6.

Zhang, H., Wu, Z., Wang, Z., Yan, X., Duan, X., Sun, H., 2025. Advanced surface modification techniques for titanium implants: a review of osteogenic and antibacterial strategies. Front. Bioeng. Biotechnol. 13. https://doi.org/10.3389/fbioe.2025.1549439.